Energy & Environmental Science

ROYAL SOCIETY OF CHEMISTRY

PAPER

View Article Online
View Journal | View Issue

Cite this: *Energy Environ. Sci.*, 2025, **18**, 8029

Understanding the reaction energetics of oxygen-evolving electrocatalysts†

Ziqing Lin,[a] Payal Chaudhary,[b] S. Avery Vigil,[a] Matteo Fratarcangeli,[a] Conner J. Soderstedt,[a] Vitaly Alexandrov[b] and Ivan A. Moreno-Hernandez *[a]

Received 20th April 2025,
Accepted 11th July 2025

DOI: 10.1039/d5ee02196k

rsc.li/ees

Electrocatalysts are crucial for efficient electrochemical devices that enable sustainable chemical transformations. Electrocatalyst activity has been correlated to the thermodynamics of reaction intermediates that balance intermediate formation and desorption. However, a lack of detailed experimental thermodynamic information about reaction energetics limits the design of next-generation electrocatalysts. Here we show kinetic and electroadsorption studies of precisely terminated first-row transition metal ruthenium oxide nanocrystals that elucidate how material chemistry influences the oxygen evolution reaction activity and reaction energetics. We established the energy scaling relations between the *OH, *O, and *OOH intermediates involved in the oxygen evolution reaction. These energy scaling relations were leveraged to design an FeMn–RuO_x electrocatalyst with an 876% increase in mass activity compared to RuO_2. Our study highlights the potential for precise nanocrystal synthesis and electroadsorption analysis to rationally guide the design of next-generation electrocatalysts with improved activity and further elucidate mechanisms of catalyst activation.

Broader context

The development of highly active electrocatalysts is vital for advancing renewable energy technologies that enable net-zero carbon emission energy and chemical infrastructures. The activity of electrocatalysts for multi-electron transfer reactions has been hypothesized to be dictated by the energetics of intermediate formation based on theoretical investigations. However, general methods to experimentally probe reaction energetics have remained elusive, preventing close integration of experimental and theoretical methods for rational catalyst design. Herein, we report electroadsorption and kinetic studies that elucidate the reaction energetics of oxygen-evolving electrocatalysts consisting of well-defined ternary first-row transition metal ruthenium oxide nanocrystals (M-RuO_x, M = V, Cr, Mn, Fe, Co, Ni, Cu, and Zn). Analysis of the electroadsorption profiles for M-RuO_x enabled the experimental measurement of intermediate binding energies that revealed energy scaling relations that exhibited linearity consistent with theoretical predictions. Electroadsorption analysis was utilized to aid the design of a quaternary transition metal ruthenium oxide electrocatalyst, FeMn-RuO_x, that exhibited higher activity towards the acidic oxygen evolution reaction compared to the most active M-RuO_x and RuO_2. Our study highlights the potential for electroadsorption analysis to elucidate the reaction energetics of complex multi-electron transfer reactions, which can accelerate the rational design of next-generation electrocatalysts with superior activity.

Introduction

Electrochemical devices powered by renewable energy enable the decarbonization of human activities to address ongoing energy and environmental challenges.[1–4] In electrolyzers, cathodic reactions that can generate fuels, commodity chemicals, and fertilizers are paired with the oxygen evolution reaction (OER), which oxidizes water molecules to form molecular oxygen *via* four electron-transfer steps.[4–9] Ruthenium dioxide (RuO_2) has been identified as one of the most promising binary oxides for the OER in acidic environments due to improved catalytic activity, but decreased stability, compared to iridium dioxide (IrO_2) and greater elemental abundance.[10–15] Efforts to further enhance the activity and stability of RuO_2 have focused on chemical, defect, and structural modulations, with a substantial body of work indicating several promising approaches to activate oxygen electrocatalysis.[13,15–23] However, to date, state-of-the-art OER electrocatalysts still exhibit lower activity than cathodic electrocatalysts for fuel formation, necessitating high OER catalyst loading in

[a] *Department of Chemistry, Duke University; Durham, North Carolina 27708, USA. E-mail: ivan.moreno-hernandez@duke.edu*
[b] *Department of Chemical and Biomolecular Engineering, University of Nebraska-Lincoln, Lincoln, Nebraska 68588, USA*

† Electronic supplementary information (ESI) available: Including supplementary results and discussion, supplementary experimental and calculation details, supplementary figures, supplementary tables. See DOI: **https://doi.org/10.1039/d5ee02196k**

devices and decreasing the scalability of electrolyzer technologies for chemical transformations.[24–29]

The slow kinetics of oxygen-evolving electrocatalysts have been attributed to non-ideal energy scaling relations of the OER intermediates (*OH, *O, and *OOH).[30–34] Seminal computational studies have explored energy scaling relations between the OER intermediates with quantum mechanical (QM) methods.[35–41] Additionally, electrochemical studies of single-crystalline RuO_2 and IrO_2 surfaces have revealed the energy scaling relations of elementary reaction steps involved in the OER *via* the analysis of electroadsorption features.[34,42–44] These approaches have provided important insights about electrocatalysts. However, understanding the OER intermediate energy scaling relations of next-generation electrocatalysts with nanoscale morphologies and complex chemical compositions remains a challenge. Recent studies have established synthetic pathways to obtain nanocrystals with precise crystallographic terminations, which have indicated that particle-to-particle heterogeneity and facet-dependent properties influence the macroscopic properties of particle ensembles.[45,46] Thus, there is a need to develop approaches to quantitatively study the energetic pathways of complex reactions such as the OER to rationally design electrocatalysts with high activity.

In this study, we report the synthesis of rutile oxide nanocrystals consisting of a first-row transition metal, ruthenium, and oxygen (M–RuO_x, M = V, Cr, Mn, Fe, Co, Ni, Cu, and Zn) and the experimental determination of energy scaling relations between the *OH, *O, and *OOH intermediates for the OER. The synthesis of M–RuO_x nanocrystals with well-defined (110) and (111)/(112) crystallographic facets and minimal structural defects enabled the determination of chemical effects on electrocatalysis. Our experiments for binary systems revealed that only Mn–RuO_x exhibits substantially improved activity compared to RuO_2 on an electrochemically-active surface-area basis. Electroadsorption analysis enabled the determination of absolute reaction energetics for the *OH, *O, and *OOH intermediates and quantification of intermediate surface coverage for all M–RuO_x nanocrystals. The energetics of the OER on (110) and (111)/(112) surfaces could be deconvoluted and revealed distinct facet-dependent energy scaling relations. The observed variation in catalytic activity for all M–RuO_x samples could be accurately described by a kinetic model that incorporates OER energetics and intermediate surface coverage determined from electroadsorption analysis. Importantly, these insights enabled the design of a ternary FeMn–RuO_x electrocatalyst that was predicted to exhibit improved activity and was experimentally validated to yield an 876% and 309% improvement in mass activity compared to RuO_2 and Mn–RuO_x, respectively. The observed enhancement in activity for FeMn–RuO_x was further validated by density functional theory (DFT) models of the OER on the (110) M–RuO_x surfaces. Overall, our study highlights the potential for electroadsorption analysis and precise nanocrystal synthesis to provide key insights that elucidate electrocatalytic reaction pathways and enable the design of next-generation electrocatalysts.

Experimental

Synthesis method of nanocrystals

All samples were prepared using a previously reported molten salt synthetic method.[46] To synthesize ruthenium dioxide (RuO_2) nanocrystals, 4.55 g of NaCl, 600 μL of 80 mM $RuCl_3$, and 500 μL of 400 mM Na_2SO_4 were added to a 10 mL ceramic crucible (470149-028, VWR International). To synthesize each ternary first-row transition metal ruthenium oxide nanocrystal sample (M–RuO_x, M = V, Cr, Mn, Fe, Co, Ni, Cu and Zn), 4.55 g of NaCl, 250 μL of 80 mM $RuCl_3$, 500 μL of 400 mM Na_2SO_4, 500 μL of deionized water, and 50 μL of 400 mM transition metal salt precursor dissolved in 2 M HCl were added to a ceramic crucible. To synthesize iron manganese ruthenium oxide (FeMn–RuO_x) nanocrystals with different atomic percentage of Fe, 4.55 g of NaCl, 250 μL of 80 mM $RuCl_3$, 500 μL of 400 mM Na_2SO_4, 500 μL of deionized water, between 15 and 50 μL of 400 mM $MnCl_2$ dissolved in 2 M HCl and between 0 and 50 μL of 400 mM of $FeCl_3$ dissolved in 2 M HCl were added to a ceramic crucible.

For RuO_2 and M–RuO_x, all the contents in the crucible were well-mixed *via* stirring and then heated at 700 °C for one hour in a box furnace with a heating rate of 20 °C min^{-1} and with natural cooling. For FeMn–RuO_x, all the contents in the crucible were well-mixed *via* stirring and then heated at 500 °C for one hour in a box furnace with a heating rate of 20 °C min^{-1} and natural cooling. After cooling down to room temperature, all samples were purified with a series of washing steps. All the washing steps were conducted by centrifuging the samples at 6000 rpm and removing the supernatant. Approximately 35 mL of water was used to transfer the contents in each crucible to a 50 mL centrifuge tube. Each sample was washed for 10 minutes to ensure total dissolution of the salt matrix. Subsequently, each sample was re-dispersed in 1 mL of 2 M HCl and transferred into a 1.5 mL microcentrifuge tube. The microcentrifuge tubes were immersed in a 90 °C hot water bath for one hour unless otherwise specified to remove any excess oxides that were unstable in acid.[17,47,48] After cooling down from the water bath, the acid supernatant was removed *via* centrifugation. Each sample was washed twice with 1 mL of water and once with 1 mL IPA, centrifuging for 5 minutes and removing the supernatant after each washing step. After all the washing steps, samples were stored in a vacuum desiccator until completely dry.

Electrochemical characterization

All electrochemical measurements were conducted using a rotating disk electrode (MSR Rotator, Pine Research) operated at 2000 rpm and a three-electrode system at room temperature (25 °C) using a digital potentiostat (Bio-logic VSP-300). The counter electrode was a platinum electrode (Pine Research), the reference electrode was an Ag/AgCl electrode (Pine Research), the working electrode was a glassy carbon rotating disk electrode (Pine Research, diameter of 5 mm), and the electrolyte was 1.0 M $HClO_4$. Ultrahigh purity oxygen was bubbled during the experiments to saturate the electrolyte. The Ag/AgCl

reference electrode was calibrated to 0.1899 V *versus* the reversible hydrogen electrode (RHE). Electrocatalyst inks were prepared for each sample as follows. For every 1 mg of nanopowder, 83.5 μL of H_2O, 35.5 μL of IPA and 6 μL of Nafion were added. The mixtures were sonicated for 40 minutes to fully suspend the particles. The catalyst inks were then drop-cast on top of a glassy carbon electrode polished to a mirror finish with 3.07 μL of synthesized catalyst ink for a loading of 125 μg cm^{-2}. The loading was repeated once for all samples, resulting in a final catalyst loading of 250 μg cm^{-2}. To characterize the electrochemical performance of the catalysts, a series of experiments were conducted. Electrochemical impedance spectroscopy (EIS) was conducted to determine the series resistance with frequency ranging from 1 MHz to 1 Hz. Next, a cyclic voltammetry (CV) protocol with potential ranges from 0 to 1.45 V *versus* Ag/AgCl was performed at scan rate (ν) descending from 1000 mV s^{-1} to 100 mV s^{-1}. A 10 mV s^{-1} scan-rate CV was performed with potential ranges from 0.95 to 1.45 V *versus* Ag/AgCl to measure the OER kinetics at steady-state.

Results and discussion

Nanocrystal synthesis and characterization

Rutile-type nanocrystals (M–RuO_x) consisting of a first-row transition metal (M = V, Cr, Mn, Fe, Co, Ni, Cu, Zn), ruthenium, and oxygen were synthesized *via* a molten salt method to elucidate chemical effects on RuO_2 electrochemical activity (Fig. 1a). While nanocrystals were synthesized with a loaded 1 : 1 M : Ru ratio, transition metal incorporation into the RuO_2 is expected to be highly element dependent.[49] A 1 : 1 ratio was chosen to maximize the amount of transition metal incorporated in the RuO_2 lattice to elucidate the maximal effects of transition metal incorporation on reaction energetics. Acid-stable electrocatalysts were obtained by treating the as-synthesized M–RuO_x nanocrystals in 2 M HCl at 90 °C for 1 hour as described in the Experimental section. Additional discussion on the influence of acid treatment on material and electrochemical properties, as well as repeated electrochemical cycling, are available in the ESI.† The RuO_2 nanocrystal exhibited preferential growth along the [001] direction and surface termination by (110) facets on the nanocrystal sides, and (111) facets at the nanocrystal tips as determined by the projected angle and the spacing of the high-resolution transmission electron microscopy (HR-TEM) pattern (Fig. 1b). Selected-area electron diffraction (SAED) indicated the formation of a rutile-type crystal structure for all M–RuO_x and RuO_2 samples (Fig. 1c and Fig. S2, ESI†). Scanning electron microscopy-based energy dispersive spectroscopy (SEM-EDS) confirmed the incorporation of all first-row transition metals in the RuO_2 lattice (Table S1, ESI†). HR-TEM images of M–RuO_x nanocrystals with first-row transition metal incorporation showed that they exhibited anisotropic structures and surface

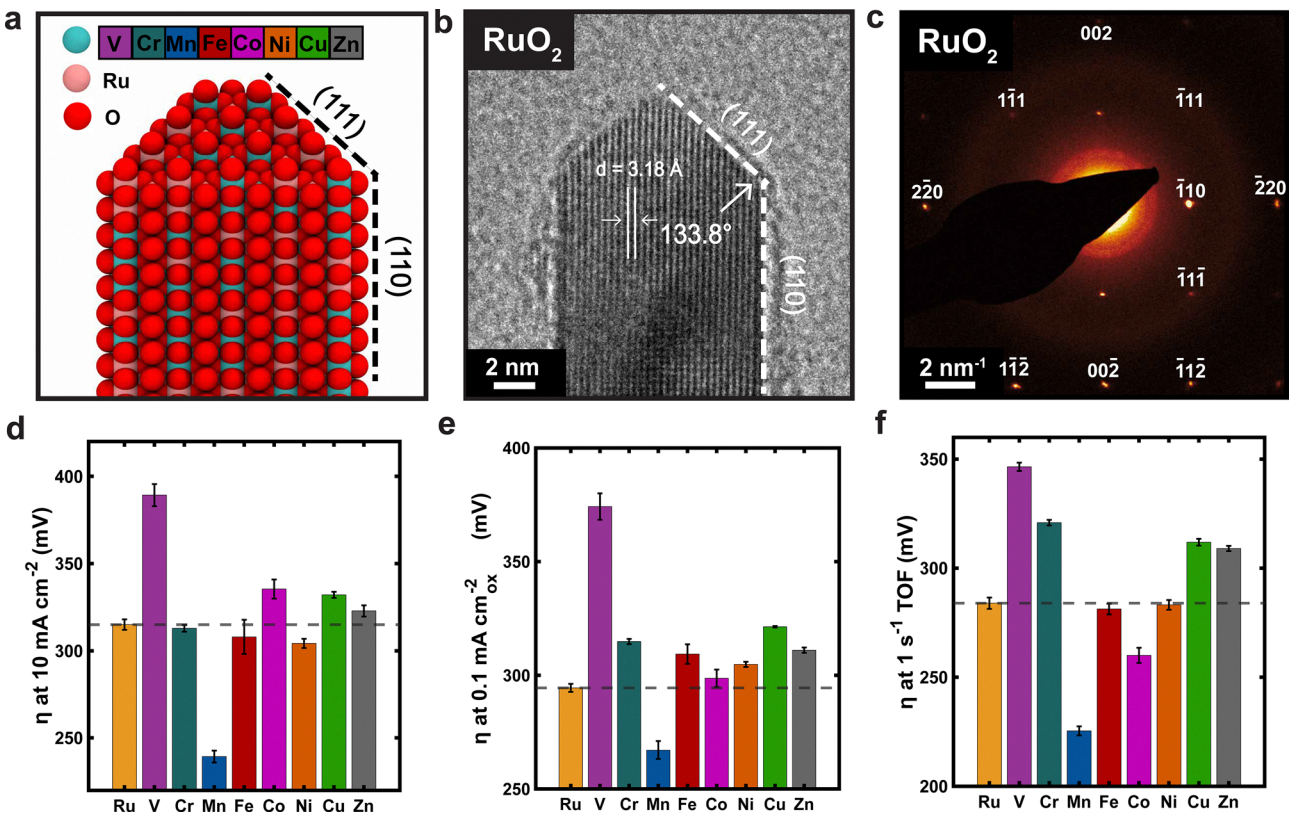

Fig. 1 Characterization of RuO_2 and M–RuO_x electrocatalysts synthesized at 700 °C. (a) Model of M–RuO_x nanocrystals. (b) HR-TEM image of RuO_2 nanocrystal with crystallographic facets and *d*-spacing labeled. (c) SAED of RuO_2 single nanocrystal shown in (b) with diffraction spots labeled. Overpotentials of all M–RuO_x compared to RuO_2 (dash line) at (d) 10 mA cm^{-2}, (e) 0.1 mA cm_{ox}^{-2}, and (f) 1 s^{-1} TOF.

faceting similar to RuO_2 with minimal structural defects (Fig. S1, ESI†). The (110) crystallographic facet was present on all M–RuO_x nanocrystal samples. The intersection angle between the nanocrystal tip and (110) facet was between 113.9 and 143.6 degrees for M–RuO_x nanocrystals, corresponding to tip terminations due to (111) and (112) crystallographic facets. X-ray diffraction (XRD) of M–RuO_x and RuO_2 confirmed the rutile-type structure and indicated that first-row transition metal incorporation resulted in changes to the rutile unit cell parameters (Fig. S3 and Table S2, ESI†). In particular, the c unit cell parameter decreased from 3.11 Å for RuO_2 to 3.08, 3.07, 3.09, and 3.09 Å for Cr–RuO_x, Mn–RuO_x, Fe–RuO_x, and Co–RuO_x, respectively. Raman spectroscopy indicated the presence of E_g, A_{1g}, and B_{2g} vibrational modes consistent with a rutile-type structure for RuO_2 nanocrystals, and similar modes with different mode positions for all M–RuO_x except Fe–RuO_x, consistent with previous observations of transition-metal incorporated RuO_2 materials (Fig. S4, ESI†).[50,51] Scanning transmission electron microscopy energy dispersive spectroscopy (STEM-EDS) confirmed the homogenous inclusion of all transition metals in the M–RuO_x lattice (Fig. S5, ESI†).

Oxygen evolution reaction activity

Fig. 1d–f summarizes the electrochemical activity towards the OER in 1.0 M perchloric acid of M–RuO_x and RuO_2 synthesized at 700 °C. The resistance corrected overpotential at 10 mA cm^{-2} of geometric area for a catalyst loading of 250 μg cm^{-2} was 315 ± 3 mV for RuO_2 (Fig. 1d, Fig. S6 and Tables S3, S4, ESI†). The overpotential for Mn–RuO_x was 239 ± 3 mV, which was the lowest among all M–RuO_x samples. Cr–RuO_x, Fe–RuO_x, and Ni–RuO_x exhibited overpotentials between 304 ± 3 and 313 ± 2 mV, indicating an improvement in activity compared to RuO_2. V–RuO_x, Co–RuO_x, Cu–RuO_x, and Zn–RuO_x exhibited a decrease in activity compared to RuO_2. In particular, V–RuO_x exhibited the highest overpotential of 389 ± 6 mV. The geometric area-normalized activity of the studied electrocatalysts could be influenced by two key factors: the surface area of the nanocrystals, and the density of active sites on a given surface. The electrochemically-active surface-area (ECSA) normalized activity is shown in Fig. 1e, Fig. S7 and Table S3 (ESI†). The overpotential at 0.1 mA per cm_{ox}^2 is 294 ± 2 mV for RuO_2. After ECSA normalization, only Mn–RuO_x exhibited higher activity than RuO_2, with an ECSA-normalized overpotential of 267 ± 4 mV. These results indicate that the enhanced activity of Cr–RuO_x, Fe–RuO_x, and Ni–RuO_x could be attributed to surface area enhancements or differences in active site density, which was determined *via* electroadsorption analysis as described in the Supplementary Methods (ESI†). The active site density of RuO_2 was 1.68 ± 0.06 sites nm^{-2}, corresponding to 33% of the available Ru coordinately unsaturated sites (CUS) on a RuO_2 (110) surface (5.1 sites nm^{-2}) (Table S5, ESI†).[52] Cr–RuO_x, Cu–RuO_x, and Zn–RuO_x exhibited site densities of between 1.61 ± 0.07 and 2.361 ± 0.003 sites nm^{-2} (Table S5, ESI†). Mn–RuO_x exhibited a site density of 0.318 ± 0.002 sites nm^{-2}, corresponding to 6.2% of the CUS sites on a RuO_2 (110) surface (Table S5, ESI†). The results indicate that site density must be accounted to determine the intrinsic activity of active sites for different electrocatalysts. The overpotential at a turnover frequency (TOF) of 1 oxygen molecule per active site accounts for both surface area and site density effects on catalysis. The overpotential at 1 s^{-1} TOF was 284 ± 3 mV for RuO_2 (Fig. 1f and Table S5, ESI†). Mn–RuO_x, Fe–RuO_x, Co–RuO_x, and Ni–RuO_x exhibited overpotentials at 1 s^{-1} TOF of 225 ± 2, 281 ± 2, 260 ± 3, and 283 ± 2 mV, indicating that their active sites exhibited higher intrinsic activity than RuO_2. V–RuO_x, Cr–RuO_x, Cu–RuO_x, and Zn–RuO_x exhibited decreased activity at 1 s^{-1} TOF compared to RuO_2. In particular, V–RuO_x exhibited the highest overpotential at 346 ± 2 mV for 1 s^{-1} TOF. Tafel slope analysis from a limited current range of 0.1 to 10 mA cm^{-2} indicated that RuO_2, Mn–RuO_x, and V–RuO_x exhibited a Tafel slope of 32.5, 19.1, and 41.7 mV dec^{-1}, and others exhibited Tafel slopes between 23.4 and 29.8 mV dec^{-1} (Fig. S8, ESI†).

Electroadsorption and kinetic analysis

Unless otherwise stated, three cyclic voltammograms were collected at 1000 mV s^{-1} and the third cyclic voltammogram was utilized for electroadsorption analysis. Fig. 2a–d summarizes electroadsorption analysis results of RuO_2 nanocrystals. Microkinetic models of the OER for all permutations of unique reaction energies verified that electroadsorption features would be observed during fast cyclic voltammetry scans (Fig. S9–S12, ESI†). In most cases, the number of features observed would be one less than the rate-determining step. Many energy combinations could be adequately described by an electroadsorption model of surface-bound electrochemical reactions (Fig. S13 and S14, ESI†). Fig. S15 (ESI†) and Fig. 2a shows cyclic voltammograms collected for M–RuO_x and RuO_2 nanocrystals at a scan rate of 1000 mV s^{-1}. The capacitive current of the cyclic voltammograms was determined as described in the Supplementary Methods (ESI†). The electroadsorption features exhibited peak broadening that could not be explained by an idealized Nernstian surface-limited process (Fig. S16a, ESI†). Recent studies have indicated that the properties of individual RuO_2 nanocrystals are highly heterogeneous and that intermediates could exhibit adsorbate–adsorbate interactions.[34,45] We developed an analytical model that could account for electroadsorption peak broadening that could be used to quantitatively describe the observed capacitive current of the electrocatalysts as discussed in the Supplementary Methods (ESI†). Fig. 2b shows the capacitive current obtained for RuO_2 nanocrystals. Electroadsorption features are observed between 0 V *vs.* RHE and ~1.45 V *vs.* RHE. The features could be separated into low-integrated-charge features below 1 V *vs.* RHE, and high-integrated-charge features above 1 V *vs.* RHE. Prior work on single crystals of RuO_2 (110) observed electroadsorption features above 1 V *vs.* RHE, and the absence of electroadsorption features below 1 V *vs.* RHE.[34] The anisotropic structure of M–RuO_x and RuO_2 results in the predominant areal exposure of (110) facets with minor contributions from (111) or other facets. Thus, we ascribe the observed features above 1 V *vs.* RHE to (110) facets and features below 1 V *vs.* RHE to (111)/(112) facets. The electroadsorption features were fit to an electroadsorption model of *OH, *O, and *OOH intermediate formation.

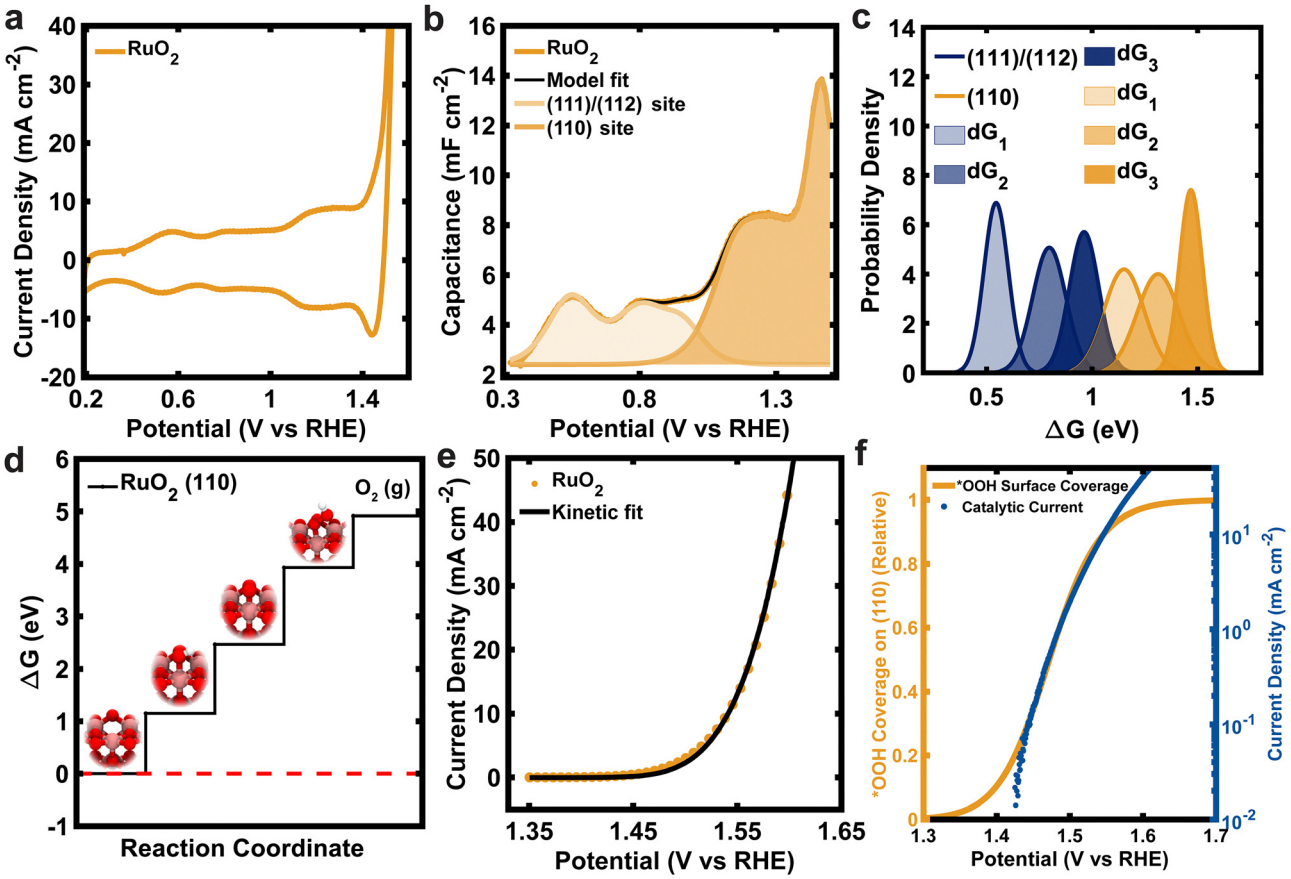

Fig. 2 Electroadsorption and kinetic analysis of RuO_2 electrocatalyst synthesized at 700 °C. (a) Cyclic voltammogram scanned at 1 V s^{-1}. (b) Comparison of electroadsorption model fits of (111)/(112) and (110) sites to electroadsorption profile derived from (a). (c) Distributions of reaction energies for the first three electron-transfer steps involved in the OER. (d) Free energy diagram constructed from electroadsorption analysis. (e) Comparison between steady-state current density and kinetic model fit. (f) Surface coverage of *OOH species on (110) site and catalytic current density *versus* potential.

Analysis of the RuO_2 capacitive current profile indicates the formation of *OH, *O, and *OOH intermediates at 1.151 ± 0.007, 1.313 ± 0.004, and 1.468 ± 0.005 V *vs.* RHE on RuO_2 (110) surfaces, and 0.545 ± 0.003, 0.797 ± 0.003, and 0.962 ± 0.003 V *vs.* RHE on RuO_2 (111)/(112) surfaces, respectively (Fig. 2b and Tables S6, S7, ESI†). Broadening of electroadsorption features could be described by collections of idealized Nernstian reactions exhibiting normal distributions with standard deviations in Gibbs free energy between 19 and 117 meV (Fig. 2c, Fig. S16b and Tables S8, S9, ESI†). The *OH surface coverage was 0.9 ± 0.1 mC cm^{-2} and 0.52 ± 0.07 mC cm^{-2} on (110) and (111)/(112) surfaces, respectively (Tables S10 and S11, ESI†). The energetics obtained from electroadsorption analysis enabled the construction of a reaction coordinate diagram for the OER from the experimental dataset (Fig. 2d). The determined binding energies for the OER intermediates on RuO_2 suggest that (110) and (111)/(112) surfaces exhibit a thermodynamic barrier of at least 239 ± 5 meV and 1380 ± 10 meV, respectively (Tables S6 and S7, ESI†). Fig. 2e and f summarizes kinetic analysis for the OER on RuO_2 nanocrystals. Substantial overlap between the formation of *OOH on the (110) surface and activity onset was observed (Fig. 2f). The overall activity could be adequately described by an electrochemical reaction with first-order electrochemical reaction kinetics with respect to *OOH on (110) crystallographic facets, which exhibit more optimal energetics for the OER compared to (111)/(112) active sites (Fig. 2e).

Fig. 3a and b shows the model analysis of M–RuO_x. Capacitive current measurements indicate that M–RuO_x electrocatalysts exhibit differences in electroadsorption compared to RuO_2 (Fig. 3a). The resulting binding energies from electroadsorption analysis enabled the construction of experimental energy scaling relations between *OH, *O, and *OOH for (110) crystallographic facets (Fig. 3c and d). The *OH binding energy ranged from 1.076 ± 0.002 to 1.209 ± 0.007 eV for (110) facets (Fig. 3c and d). A linear fit of the *O binding energy *versus* the *OH resulted in a slope of 1.66, and an offset of 0.56 eV (Fig. 3c). A linear fit of the *OOH binding energy *versus* the *OH resulted in a slope of 1.98, and an offset of 1.64 eV (Fig. 3d). Similar analysis was conducted for active sites modeled by (111)/(112) crystallographic facets (Fig. S17a and b, ESI†). Electroadsorption analysis of the resulting scaling laws indicates that (111)/(112) facets for M–RuO_x and RuO_2 exhibit thermodynamics barriers that are non-ideal for the OER (Table S6, ESI†). The thermodynamic barrier for Mn–RuO_x (110), 185 ± 1 meV, is close to the predicted optimum for the OER, 166 meV, based on the determined scaling law for *O and *OOH (Fig. S17c, ESI†).

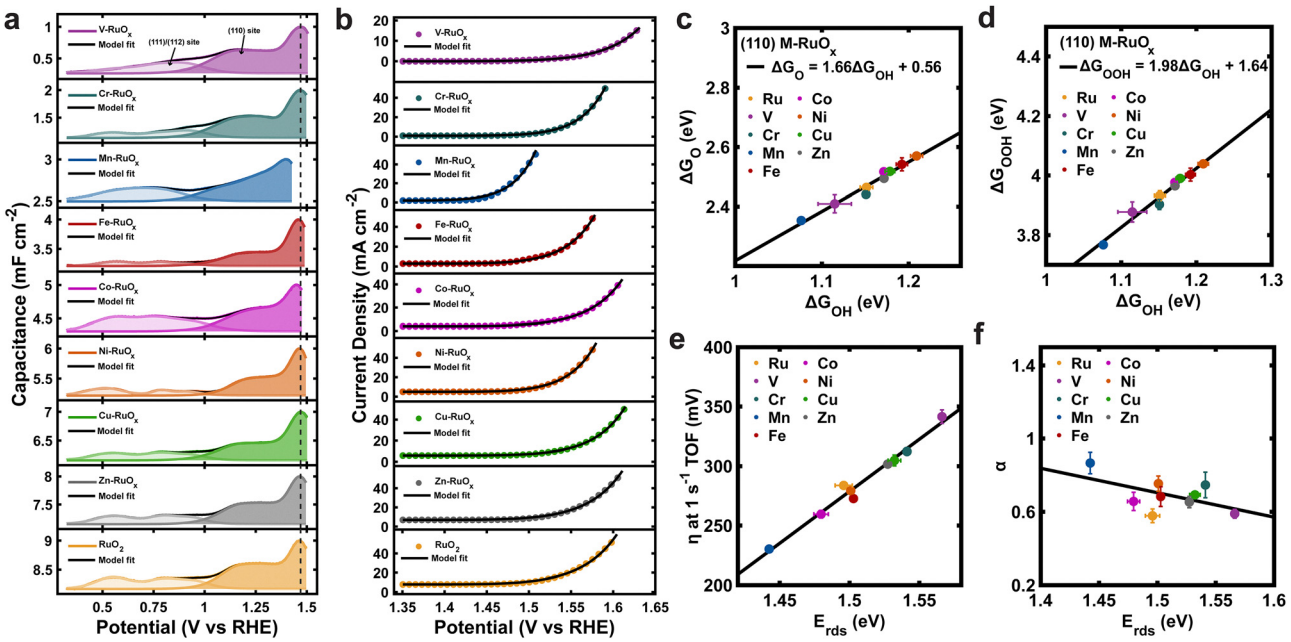

Fig. 3 Electroadsorption and kinetic analysis of M–RuO_x electrocatalysts synthesized at 700 °C. (a) Comparison of electroadsorption model fits of (111)/(112) and (110) sites to electroadsorption profiles for M–RuO_x. (b) Comparison between steady-state current density and kinetic model fits for M–RuO_x. Experimentally derived scaling relations of (c) ΔG_O *versus* ΔG_{OH} and (d) ΔG_{OOH} *versus* ΔG_{OH} on (110) site. (e) Overpotential at 1 s^{-1} TOF *versus* E_{rds}. (f) Charge-transfer coefficient α *versus* E_{rds}.

Electroadsorption analysis indicated that Fe–RuO_x, Co–RuO_x, Ni–RuO_x, Cu–RuO_x, Zn–RuO_x destabilized the *OH, *O, and *OOH intermediates, and Mn–RuO_x, V–RuO_x, Cr–RuO_x stabilized the intermediates (Fig. S17d and e, ESI†). Prior DFT results indicate that for *OH binding energies between 1.0 eV and 1.2 eV, corresponding to the binding energies measured herein for M–RuO_x, the binding energies for *O can vary between 2.4 eV and 4.4 eV.[53] In these prior studies, the *OOH binding energy was found to vary between 3.6 eV and 4.7 eV in the 1.0 eV to 1.2 eV *OH binding energy range.[53] Our electroadsorption studies indicate that experimental *O and *OOH binding energies fall within this range (Fig. 3c and d). The kinetic profiles of M–RuO_x were found to be adequately described by first-order kinetic rate laws with a rate-determining step of *OOH oxidation to O_2 (Fig. 3b). Analysis of the resulting kinetic parameters indicates that the activation barrier of the rate-determining step is correlated to the overpotential at 1 s^{-1} TOF and the charge transfer coefficient (α) (Fig. 3e and f).

Design of quaternary oxide electrocatalyst

Fig. 4 demonstrates the design of a quaternary oxide OER electrocatalyst based on electroadsorption analysis. Mn–RuO_x was found to exhibit the highest intrinsic activity towards the oxygen evolution reaction, but also the lowest density of active sites. The interaction between first-row transition metals in a RuO_2 lattice is highly complex, and electroadsorption analysis was used to understanding potential synergistic effects in the Fe–Mn–Ru–O chemical space. Our motivation for exploring this combination came from the observed decrease in Gibbs free energy for the *O to *OOH transition (Table S7, ESI†) for both Mn–RuO_x and Fe–RuO_x, and the increase in active site density for Fe–RuO_x compared to Mn–RuO_x (Table S5, ESI†). Nanocrystals consisting of solid solutions between Fe–RuO_x and Mn–RuO_x, and RuO_2, were synthesized at 500 °C. XPS and SEM-EDS analysis confirms the inclusion of Mn, Fe, and Ru in the Mn(II), Fe(II), and Ru(IV) oxidation states, respectively, in the FeMn–RuO_x nanocrystals (Fig. S20 and Table S1, ESI†). XPS studies indicate the Ru, Mn, and Fe remain in the (IV), (II) and (II) oxidation states after electrochemical operation for 3 cyclic voltammograms between 0.00 V and 1.45 V *vs.* Ag/AgCl at 1000 mV s^{-1} (Fig. S20, ESI†). Fig. S21a (ESI†) shows the HR-TEM image of the FeMn–RuO_x nanocrystal. The FeMn–RuO_x nanocrystal exhibited anisotropic structures and surface faceting similar to RuO_2, indicated by the (110) crystallographic facet. SAED and XRD of FeMn–RuO_x indicated a rutile-type crystal structure (Fig. S21b and c, ESI†).

Three cyclic voltammograms were collected at 1000 mV s^{-1} and three cyclic voltammograms were collected at 500 mV s^{-1}. The third cyclic voltammogram collected at 500 mV s^{-1} was utilized for electroadsorption analysis. Electroadsorption analysis indicated that nanocrystals with both Fe and Mn exhibited cooperative intermediate stabilization as indicated by a decrease in *OH, *O, and *OOH binding energies that could not be described as a linear combination of Fe–RuO_x and Mn–RuO_x binding energies (Fig. 4a, d and Fig. S22, ESI†). This cooperative stabilization resulted in a different scaling relation for OER intermediates on (110) Fe–Mn–Ru rutile surfaces with a slope of 1.90 and an intercept of 0.28 eV for *O *vs.* *OH, and a slope of 2.22 and intercept of 1.32 eV for

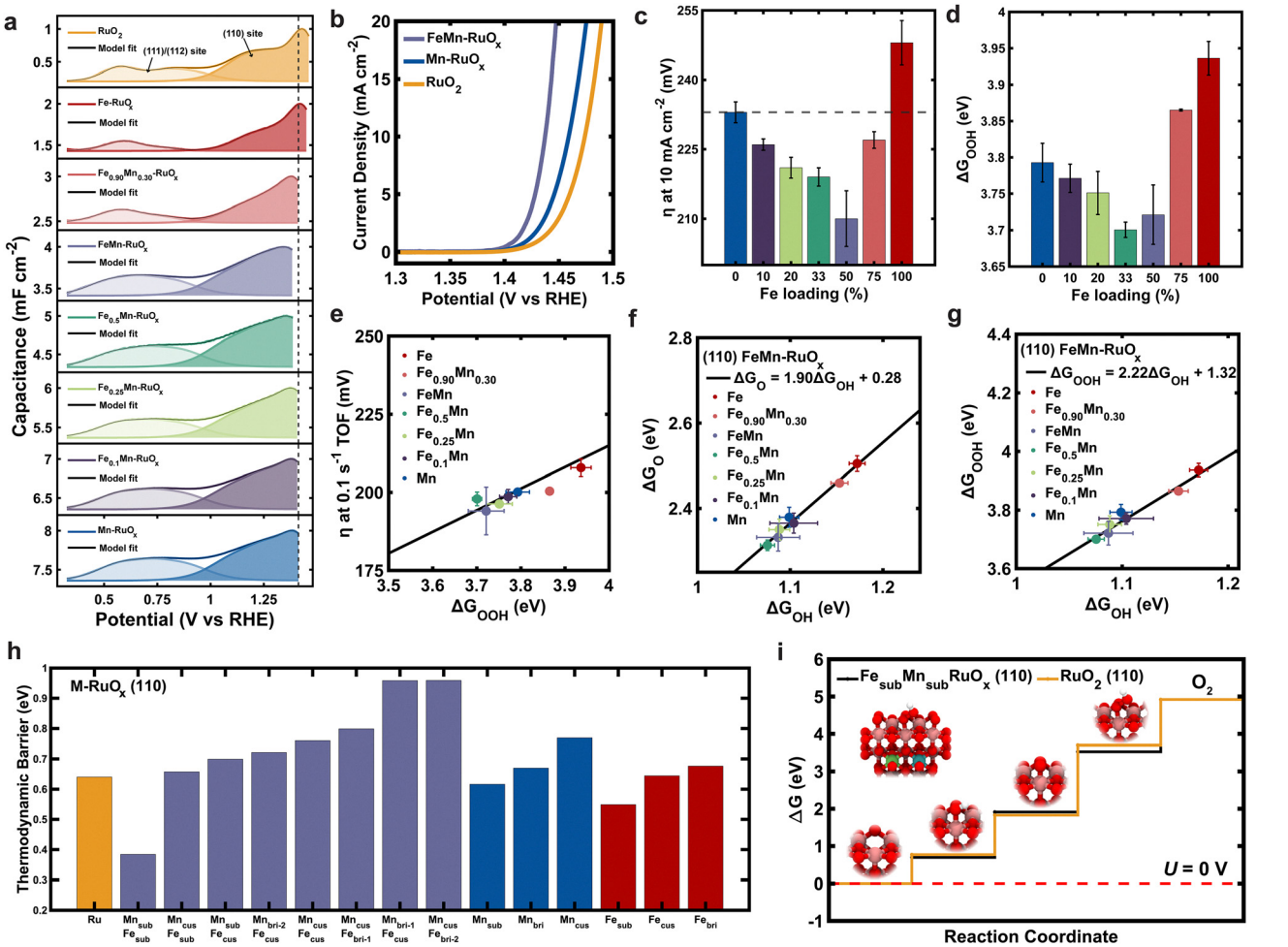

Fig. 4 Summary of electroadsorption and DFT analysis of FeMn–RuO$_x$ electrocatalysts with different Fe loading [Fe/(Fe + Mn)] synthesized at 500 °C. (a) Comparison of electroadsorption model fits of (111)/(112) and (110) sites to electroadsorption profiles for FeMn–RuO$_x$ electrocatalysts. (b) Steady-state current density of FeMn–RuO$_x$, Mn–RuO$_x$, and RuO$_2$ synthesized at 500 °C. (c) Overpotentials at 10 mA cm^{-2} for different Fe loading of FeMn–RuO$_x$ [Fe/(Fe + Mn)]. (d) ΔG_{OOH} on (110) site for different Fe loading of FeMn–RuO$_x$. (e) Overpotentials at 0.1 s^{-1} TOF *versus* ΔG_{OOH} on (110) site for different Fe loading of FeMn–RuO$_x$. Scaling relations for (110) site of (f) ΔG_O *versus* ΔG_{OH} and (g) ΔG_{OOH} *versus* ΔG_{OH}. (h) DFT calculated thermodynamic overpotentials for M–RuO$_x$ (M = Ru, Fe, Mn) on (110) surface. See the corresponding atomic configurations in Fig. S24 (ESI†). (i) Free energy diagram of Fe$_{sub}$Mn$_{sub}$RuO$_x$ and RuO$_2$ on (110) site constructed from DFT calculations.

*OOH *vs.* *OH (Fig. 4f and g). Our studies indicate that M–RuO$_x$ nanocrystals exhibit a linear correlation of *O *versus* *OH with a slope of 1.66, and that FeMn–RuO$_x$ nanocrystals exhibit a corresponding slope of 1.9 (Fig. 3c and 4f). Prior DFT results, summarizing a decade of atomic scale simulations, indicate *O *versus* *OH slopes of 1.6 for all considered samples, closely matching our observed scaling relation.[53] Additionally, heavily doped samples with more than 1 dopant exhibit a slope of 1.75, and 2-dopant TiO$_2$ exhibits a slope of 1.9.[53] Prior studies comparing measured electroadsorption energies for single-crystalline RuO$_2$(110) surfaces with DFT results have highlighted challenges in reproducing exact energies with DFT due to approximations in the theoretical technique.[34] In general, our electroadsorption studies on M–RuO$_x$ and FeMn–RuO$_x$ agree well with the observed trends from prior DFT results and provide key experimental findings for the development of more accurate atomic scale simulations.

Kinetic analysis indicated that activity could be attributed to (110) Fe–Mn–Ru rutile surfaces (Fig. S23 and Tables S6, S7, S12, ESI†). This new scaling relation resulted in more ideal thermodynamics for the OER, and FeMn–RuO$_x$ exhibited a thermodynamic barrier of 160 ± 9 meV, which is 25 meV lower than the most active Mn–RuO$_x$ binary oxide (Table S7, ESI†). Fig. 4b shows the electrocatalytic activity of FeMn–RuO$_x$ (1 : 1 Fe : Mn) compared to Mn–RuO$_x$ and RuO$_x$ synthesized under the same conditions. A synthesis ratio of 1 : 1 Fe : Mn was found to optimize the activity of FeMn–RuO$_x$-based electrocatalysts, consistent with the measured intermediate binding energies (Fig. 4c and Table S7, ESI†). The overpotential at 10 mA cm^{-2} for RuO$_2$, Mn–RuO$_x$, and the optimized FeMn–RuO$_x$ synthesized at 500 °C was 250 ± 2, 233 ± 2 and 210 ± 6 mV, respectively (Table S3 and Fig. S19, ESI†). Fig. 4h demonstrates DFT analysis of rutile (110) surfaces for the Fe–Mn–Ru–O chemical space. Mn and Fe inclusion in RuO$_2$ (110) surfaces

could occur at CUS, bridge, and subsurface sites as indicated in Fig. S24 (ESI†). Analysis of the OER reaction energetics with DFT indicates that the thermodynamic OER overpotentials are highly sensitive to doping location, and that doping also influences the relative stability of the (110) surface (Fig. 4h and Table S14, ESI†). Overall, our DFT results support the experimental finding of improved OER activity of the FeMn–RuO_x system in the case of subsurface Fe and Mn dopants (Fe_{sub}–Mn_{sub}) (Fig. 4h and i).

The electrochemical degradation of Ru-based electrocatalysts impedes widescale implementation in electrolyzer technologies.[22,54] Proton exchange membrane water electrolysis (PEMWE) devices constructed with FeMn–RuO_x and RuO_2 to determine electrocatalyst activity and stability under realistic operation conditions are shown in Fig. S21 (ESI†). Catalyst-coated membranes were prepared on Nafion N115 to determine FeMn–RuO_x and RuO_2 electrocatalyst stability. FeMn–RuO_x exhibited stable operation with a potential below 1.65 V for over 200 hours of operation at 100 mA cm^{-2}. A RuO_2-based electrolyzer exhibited a potential above 1.8 V after 180 hours of operation, indicating operational instability after long-term electrolysis. Catalytic activity towards water electrolysis was further verified with electrolyzers optimized for activity by utilizing a thinner Nafion N212 membrane and 80 °C water feed. Thin membranes can result in membrane-induced device degradation but can be utilized to evaluate next generation electrolyzer performance.[55] Our results indicate that the FeMn–RuO_x electrocatalyst can achieve 1 A cm^{-2} at 1.58 V, and a current density of 6.54 A cm^{-2} at 2.0 V, surpassing the activity of commercial RuO_2 (Fig. S21, ESI†). The device-scale Ru mass activity of the FeMn–RuO_x electrolyzer was found to be 143.2% higher than the mass activity of the RuO_2 electrolyzer at 2 V, consistent with the high mass activity observed in three-electrode experiments.

Conclusion

The energy scaling relations of intermediates involved in electrochemical reactions with multiple reaction steps limit catalyst activity and complicate material design. In this work, we demonstrated that the electroadsorption profile of electrocatalyst materials could be quantitatively analyzed to obtain reaction energetics. Systematic changes in RuO_2 nanocrystal chemistry enabled the study of chemical effects on the OER energetics and the experimental determination of energy scaling relations between *OH, *O, and *OOH intermediates. We expect that the precise determination of reaction energetics from experiments will accelerate the discovery of electrocatalysts and help bridge the gap between experiment and theoretical predictions. In particular, our study revealed that Mn inclusion resulted in a substantial enhancement in catalyst activity for Ru-based oxygen-evolving electrocatalysts, and that this enhancement was associated with the stabilization of the *OOH intermediate to a more favorable energy. The activity could be further improved *via* the incorporation of Fe to form an FeMn–RuO_x electrocatalyst, which exhibited cooperative stabilization of *OOH and an 876% increase in mass activity compared to RuO_2. The principles applied in this study are universal, and we expect that electroadsorption analysis will be useful for other multi-electron reactions and to understand other mechanisms of catalyst activation.

Author contributions

I. A. M.-H. and Z. L. conceived and designed the project. Z. L., S. A. V., M. F., C. J. S. conducted the experiments and collected the data. I. A. M.-H. and Z. L. analyzed and discussed the data. Z. L. and I. A. M.-H. wrote the manuscript. P. C. and V. A. contributed density functional theory results and discussion. The project was supervised by I. A. M.-H. All authors provided feedback on the manuscript.

Conflicts of interest

The authors declare no competing interest.

Data availability

Data supporting this article have been included as part of the ESI.†

Acknowledgements

This work was supported by a CAREER Award in the Chemical Catalysis program from the National Science Foundation (Award CHE-2441703). V. A. acknowledges the National Science Foundation support through the NSF CAREER award (Award CBET-1941204). S. A. V. acknowledges a National Science Foundation Research Grant Fellowship under grant no. DGE-2139754. This work was performed in part at the Duke University Shared Materials Instrumentation Facility (SMIF), a member of the North Carolina Research Triangle Nanotechnology Network (RTNN), which is supported by the National Science Foundation (award no. ECCS-2025064) as part of the National Nanotechnology Coordinated Infrastructure (NNCI). This work was performed in part at the Analytical Instrumentation Facility (AIF) at North Carolina State University, which is supported by the state of North Carolina and the National Science Foundation (award no. ECCS-2025064 and award no. ECCS-1542015). This work made use of instrumentation at AIF acquired with support from the National Science Foundation (DMR-1726294). The AIF is a member of the North Carolina RTNN, a site in the NNCI. We also acknowledge computational resources provided by the Holland Computing Center at the University of Nebraska-Lincoln.

References

1 J. A. Turner, *Science*, 2004, **305**, 972–974.
2 S. Chu and A. Majumdar, *Nature*, 2012, **488**, 294–303.
3 J. A. Turner, *Science*, 1999, **285**, 687–689.

4 Z. W. Seh, J. Kibsgaard, C. F. Dickens, I. Chorkendorff, J. K. Nørskov and T. F. Jaramillo, *Science*, 2017, **355**, aad4998.
5 M. G. Walter, E. L. Warren, J. R. McKone, S. W. Boettcher, Q. Mi, E. A. Santori and N. S. Lewis, *Chem. Rev.*, 2010, **110**, 6446–6473.
6 R. Francke, B. Schille and M. Roemelt, *Chem. Rev.*, 2018, **118**, 4631–4701.
7 J. Song, C. Wei, Z.-F. Huang, C. Liu, L. Zeng, X. Wang and Z. J. Xu, *Chem. Soc. Rev.*, 2020, **49**, 2196–2214.
8 G. T. K. K. Gunasooriya and J. K. Nørskov, *ACS Energy Lett.*, 2020, **5**, 3778–3787.
9 S. Shiva Kumar and V. Himabindu, *Mater. Sci. Energy Technol.*, 2019, **2**, 442–454.
10 H. Over, *Chem. Rev.*, 2012, **112**, 3356–3426.
11 E. A. Paoli, F. Masini, R. Frydendal, D. Deiana, C. Schlaup, M. Malizia, T. W. Hansen, S. Horch, I. E. L. Stephens and I. Chorkendorff, *Chem. Sci.*, 2015, **6**, 190–196.
12 Z.-Y. Wu, F.-Y. Chen, B. Li, S.-W. Yu, Y. Z. Finfrock, D. M. Meira, Q.-Q. Yan, P. Zhu, M.-X. Chen, T.-W. Song, Z. Yin, H.-W. Liang, S. Zhang, G. Wang and H. Wang, *Nat. Mater.*, 2023, **22**, 100–108.
13 Y. Yao, S. Hu, W. Chen, Z.-Q. Huang, W. Wei, T. Yao, R. Liu, K. Zang, X. Wang, G. Wu, W. Yuan, T. Yuan, B. Zhu, W. Liu, Z. Li, D. He, Z. Xue, Y. Wang, X. Zheng, J. Dong, C.-R. Chang, Y. Chen, X. Hong, J. Luo, S. Wei, W.-X. Li, P. Strasser, Y. Wu and Y. Li, *Nat. Catal.*, 2019, **2**, 304–313.
14 R. R. Rao, M. J. Kolb, L. Giordano, A. F. Pedersen, Y. Katayama, J. Hwang, A. Mehta, H. You, J. R. Lunger, H. Zhou, N. B. Halck, T. Vegge, I. Chorkendorff, I. E. L. Stephens and Y. Shao-Horn, *Nat. Catal.*, 2020, **3**, 516–525.
15 N.-T. Suen, S.-F. Hung, Q. Quan, N. Zhang, Y.-J. Xu and H. M. Chen, *Chem. Soc. Rev.*, 2017, **46**, 337–365.
16 L. Li, G. Zhang, C. Zhou, F. Lv, Y. Tan, Y. Han, H. Luo, D. Wang, Y. Liu, C. Shang, L. Zeng, Q. Huang, R. Zeng, N. Ye, M. Luo and S. Guo, *Nat. Commun.*, 2024, **15**, 4974.
17 D. Zhang, M. Li, X. Yong, H. Song, G. I. N. Waterhouse, Y. Yi, B. Xue, D. Zhang, B. Liu and S. Lu, *Nat. Commun.*, 2023, **14**, 2517.
18 A. Ali, F. Long and P. K. Shen, *Electrochem. Energy Rev.*, 2022, **5**, 1.
19 S. Chen, H. Huang, P. Jiang, K. Yang, J. Diao, S. Gong, S. Liu, M. Huang, H. Wang and Q. Chen, *ACS Catal.*, 2020, **10**, 1152–1160.
20 Y. Qin, T. Yu, S. Deng, X.-Y. Zhou, D. Lin, Q. Zhang, Z. Jin, D. Zhang, Y.-B. He, H.-J. Qiu, L. He, F. Kang, K. Li and T.-Y. Zhang, *Nat. Commun.*, 2022, **13**, 3784.
21 Y. Wen, P. Chen, L. Wang, S. Li, Z. Wang, J. Abed, X. Mao, Y. Min, C. T. Dinh, P. D. Luna, R. Huang, L. Zhang, L. Wang, L. Wang, R. J. Nielsen, H. Li, T. Zhuang, C. Ke, O. Voznyy, Y. Hu, Y. Li, W. A. Goddard Iii, B. Zhang, H. Peng and E. H. Sargent, *J. Am. Chem. Soc.*, 2021, **143**, 6482–6490.
22 J. Zhang, X. Fu, S. Kwon, K. Chen, X. Liu, J. Yang, H. Sun, Y. Wang, T. Uchiyama, Y. Uchimoto, S. Li, Y. Li, X. Fan, G. Chen, F. Xia, J. Wu, Y. Li, Q. Yue, L. Qiao, D. Su, H. Zhou, W. A. Goddard and Y. Kang, *Science*, 2025, **387**, 48–55.
23 C. Zheng, B. Huang, X. Liu, H. Wang and L. Guan, *Inorg. Chem. Front.*, 2024, **11**, 1912–1922.
24 B. You and Y. Sun, *Acc. Chem. Res.*, 2018, **51**, 1571–1580.
25 Y. Jiao, Y. Zheng, M. Jaroniec and S. Z. Qiao, *Chem. Soc. Rev.*, 2015, **44**, 2060–2086.
26 J. Fan, M. Chen, Z. Zhao, Z. Zhang, S. Ye, S. Xu, H. Wang and H. Li, *Nat. Energy*, 2021, **6**, 475–486.
27 H. Sun, Z. Yan, F. Liu, W. Xu, F. Cheng and J. Chen, *Adv. Mater.*, 2020, **32**, 1806326.
28 Y. Lee, J. Suntivich, K. J. May, E. E. Perry and Y. Shao-Horn, *J. Phys. Chem. Lett.*, 2012, **3**, 399–404.
29 D. Wu, Y. Wei, X. Ren, X. Ji, Y. Liu, X. Guo, Z. Liu, A. M. Asiri, Q. Wei and X. Sun, *Adv. Mater.*, 2018, **30**, 1705366.
30 Y. Guo, T. Park, J. W. Yi, J. Henzie, J. Kim, Z. Wang, B. Jiang, Y. Bando, Y. Sugahara, J. Tang and Y. Yamauchi, *Adv. Mater.*, 2019, **31**, 1807134.
31 A. J. Medford, A. Vojvodic, J. S. Hummelshøj, J. Voss, F. Abild-Pedersen, F. Studt, T. Bligaard, A. Nilsson and J. K. Nørskov, *J. Catal.*, 2015, **328**, 36–42.
32 M. T. M. Koper, *J. Electroanal. Chem.*, 2011, **660**, 254–260.
33 V. Viswanathan, H. A. Hansen, J. Rossmeisl and J. K. Nørskov, *ACS Catal.*, 2012, **2**, 1654–1660.
34 D.-Y. Kuo, H. Paik, J. Kloppenburg, B. Faeth, K. M. Shen, D. G. Schlom, G. Hautier and J. Suntivich, *J. Am. Chem. Soc.*, 2018, **140**, 17597–17605.
35 J. Greeley, *Annu. Rev. Chem. Biomol. Eng.*, 2016, **7**, 605–635.
36 J. K. Nørskov, T. Bligaard, J. Rossmeisl and C. H. Christensen, *Nat. Chem.*, 2009, **1**, 37–46.
37 I. C. Man, H.-Y. Su, F. Calle-Vallejo, H. A. Hansen, J. I. Martínez, N. G. Inoglu, J. Kitchin, T. F. Jaramillo, J. K. Nørskov and J. Rossmeisl, *ChemCatChem*, 2011, **3**, 1159–1165.
38 Y. Zhu, Z. He, Y. Choi, H. Chen, X. Li, B. Zhao, Y. Yu, H. Zhang, K. A. Stoerzinger, Z. Feng, Y. Chen and M. Liu, *Nat. Commun.*, 2020, **11**, 4299.
39 T. Reier, H. N. Nong, D. Teschner, R. Schlögl and P. Strasser, *Adv. Energy Mater.*, 2017, **7**, 1601275.
40 L. G. V. Briquet, M. Sarwar, J. Mugo, G. Jones and F. Calle-Vallejo, *ChemCatChem*, 2017, **9**, 1261–1268.
41 S. Back, K. Tran and Z. W. Ulissi, *ACS Catal.*, 2019, **9**, 7651–7659.
42 D.-Y. Kuo, J. K. Kawasaki, J. N. Nelson, J. Kloppenburg, G. Hautier, K. M. Shen, D. G. Schlom and J. Suntivich, *J. Am. Chem. Soc.*, 2017, **139**, 3473–3479.
43 L. Zhang, J. Kloppenburg, C.-Y. Lin, L. Mitrovic, S. Gelin, I. Dabo, D. G. Schlom, J. Suntivich and G. Hautier, *J. Phys. Chem. C*, 2025, **129**, 4043–4051.
44 R. R. Rao, M. J. Kolb, N. B. Halck, A. F. Pedersen, A. Mehta, H. You, K. A. Stoerzinger, Z. Feng, H. A. Hansen, H. Zhou, L. Giordano, J. Rossmeisl, T. Vegge, I. Chorkendorff, I. E. L. Stephens and Y. Shao-Horn, *Energy Environ. Sci.*, 2017, **10**, 2626–2637.
45 S. A. Vigil and I. A. Moreno-Hernandez, *J. Am. Chem. Soc.*, 2024, **146**, 11133–11140.
46 M. Fratarcangeli, S. A. Vigil, Z. Lin, C. J. Soderstedt and I. A. Moreno-Hernandez, *Matter*, 2025, **8**, 101909.
47 X. Huang, C. Lee, Y. Li, J. Xu and D. Liu, *ACS Appl. Nano Mater.*, 2024, **7**, 9244–9251.
48 J. Shim, K. Lee, Y. Yu, H. S. Lee, H. Shin, K.-S. Lee, M. S. Bootharaju, S. Han, G. S. Yi, H. Ko, S. Lee, J. Ryu,

M. Kim, B.-H. Lee, T. Hyeon and Y.-E. Sung, *J. Am. Chem. Soc.*, 2025, **147**, 16179–16188.
49 H. Sun and W. Jung, *J. Mater. Chem.*, 2021, **9**, 15506–15521.
50 Y. Lin, Z. Tian, L. Zhang, J. Ma, Z. Jiang, B. J. Deibert, R. Ge and L. Chen, *Nat. Commun.*, 2019, **10**, 162.
51 Y. Tian, S. Wang, E. Velasco, Y. Yang, L. Cao, L. Zhang, X. Li, Y. Lin, Q. Zhang and L. Chen, *iScience*, 2020, **23**, 100756.
52 K. A. Stoerzinger, L. Qiao, M. D. Biegalski and Y. Shao-Horn, *J. Phys. Chem. Lett.*, 2014, **5**, 1636–1641.
53 S. Divanis, T. Kutlusoy, I. M. Ingmer Boye, I. C. Man and J. Rossmeisl, *Chem. Sci.*, 2020, **11**, 2943–2950.
54 M. Fratarcangeli, S. A. Vigil and I. A. Moreno-Hernandez, *J. Phys. Chem. C*, 2025, **129**, 7612–7624.
55 C. R. Wang, J. M. Stansberry, R. Mukundan, H.-M. J. Chang, D. Kulkarni, A. M. Park, A. B. Plymill, N. M. Firas, C. P. Liu, J. T. Lang, J. K. Lee, N. E. Tolouei, Y. Morimoto, C. H. Wang, G. Zhu, J. Brouwer, P. Atanassov, C. B. Capuano, C. Mittelsteadt, X. Peng and I. V. Zenyuk, *Chem. Rev.*, 2025, **125**, 1257–1302.

